









Properties of Host Galaxies of Submillimeter Sources as Revealed by JWST Early Release Observations in SMACS J0723.3–7327

Cheng Cheng^{1,2,8} , Haojing Yan³ , Jia-Sheng Huang^{1,4} , Christopher N. A. Willmer⁵ , Zhiyuan Ma⁶ , and Gustavo Orellana-González⁷ 

¹ Chinese Academy of Sciences South America Center for Astronomy, National Astronomical Observatories, CAS, Beijing 100101, People's Republic of China
chengcheng@nao.cas.cn

² CAS Key Laboratory of Optical Astronomy, National Astronomical Observatories, Chinese Academy of Sciences, Beijing 100101, People's Republic of China

³ Department of Physics and Astronomy, University of Missouri, Columbia, MO 65211, USA

⁴ Center for Astrophysics, Harvard & Smithsonian | Cambridge, MA 02138, USA

⁵ Steward Observatory, University of Arizona, 933 N Cherry Avenue, Tucson, AZ 85721-0009, USA

⁶ Department of Astronomy, University of Massachusetts, Amherst, MA 01003, USA

⁷ Instituto de Investigación Interdisciplinaria, Universidad de Talca, Avenida Lircay, Talca, Chile

Received 2022 July 17; revised 2022 August 20; accepted 2022 August 26; published 2022 September 9

Abstract

Using the 0.9–4.4 μm imaging data from the James Webb Space Telescope (JWST) early release observation in the SMACS J0723.3–7327 galaxy cluster field, we discuss the properties of three submillimeter galaxies (SMGs) detected by the Atacama Large Millimeter/submillimeter Array. These sources are magnified by $1.4\text{--}2.1\times$ due to gravitational lensing. This is the first time that submillimeter galaxy hosts are resolved in the rest-frame near-infrared (NIR). One source was previously undetected by Hubble Space Telescope, while the remaining two are disk galaxies with Sérsic indices of ~ 0.9 and star formation rates on or just below the star formation “main sequence.” Their submillimeter emission originates from the inner parts of the hosts, suggesting that their dust contents are concentrated toward the center. The host half-light radii measured in the rest-frame NIR are $\sim 1.5\times$ smaller than those measured in the rest-frame optical, consistent with a concentrated dust distribution. The more severe extinction that optical light suffers toward the center makes it seemingly less concentrated. Therefore, we expect that the optically based determination of the stellar mass distribution within host galaxies could still be severely biased by dust. Interestingly, these two disk galaxies are dramatically different in their outer regions, with one being star forming and the other being quiescent. Upcoming JWST observations of statistically significant samples of SMGs will allow us to understand the correlation between the dusty star-forming regions and their hosts.

Unified Astronomy Thesaurus concepts: Far infrared astronomy (529); Luminous infrared galaxies (946); High angular resolution (2167); Infrared Astronomical Satellite (785); Infrared telescopes (794); Infrared sources (793); Galaxy clusters (584)

1. Introduction

The submillimeter galaxies (SMGs; Smail et al. 1998; Blain et al. 2002) are a population of high redshift, massive (Dudzevičiūtė et al. 2020), gas-rich (Tacconi et al. 2006; Riechers et al. 2010), and high star formation rate (SFR; Barger et al. 2014) galaxies, with considerable emission in the submillimeter (Casey et al. 2014), as a consequence of the high dust grain attenuation. Meanwhile, the SMGs are also associated with active galactic nuclei (Ueda et al. 2018).

In spite of the intense study of the SMGs in the past two decades, these galaxies are still poorly understood because of their dusty nature. In addition, due to their high redshifts and dust extinction, the observed photometry in the optical bands data are probing SMGs in the rest-frame UV, which also limits the ability to constrain the spectral energy distribution (SED) and derived properties such as the photometric redshift (photo z) and stellar mass (M_*). Previous SMG morphology studies found that SMGs are mainly disk (Toft et al. 2014). Because

the Hubble Space Telescope (HST) imaging only probes SMGs out to the rest-frame B to V bands, the compact starburst in the central dusty region (Fujimoto et al. 2017; Gullberg et al. 2019) may also lead to a flat morphology. The Spitzer/IRAC images have been fundamental to study the stellar properties of SMGs (e.g., Shanks et al. 2021), but do have a limitation because of the image resolution of $\sim 2''$, so that SMGs are frequently blended in the deep IRAC images, preventing us from accurately measuring the SEDs and spatial properties.

The recent launch and the early release observations (ERO; Pontoppidan et al. 2022) of the James Webb Space Telescope (JWST) provide a new window to explore SMGs in unrivaled depth and resolution in the mid-infrared (MIR; $\lambda_{\text{rest}} > 2.5\ \mu\text{m}$). The ERO of the JWST contains observations of the Reionization Lensing Cluster Survey (RELICS; Coe et al. 2019) cluster SMACS J0723.3–7327 (hereafter SMACS 0723) at $z = 0.4$. Prior HST observations of SMACS 0723 used the HST/ACS camera in the F435W, F606W, F814W band, and the WFC3 camera in the F105W, F125W, F140W, F160W. All the HST images reach to about 26.5 AB mag. SMACS 0723 is also mapped by the Spitzer Reionization Lensing Cluster Survey (SRELICS⁹, PI: Bradač), and the Atacama Large Millimeter Array/submillimeter Array (ALMA) Lensing Cluster Survey

⁸ Corresponding author.



Original content from this work may be used under the terms of the [Creative Commons Attribution 4.0 licence](https://creativecommons.org/licenses/by/4.0/). Any further distribution of this work must maintain attribution to the author(s) and the title of the work, journal citation and DOI.

⁹ <https://www.ipac.caltech.edu/doi/irsa/10.26131/IRSA426>

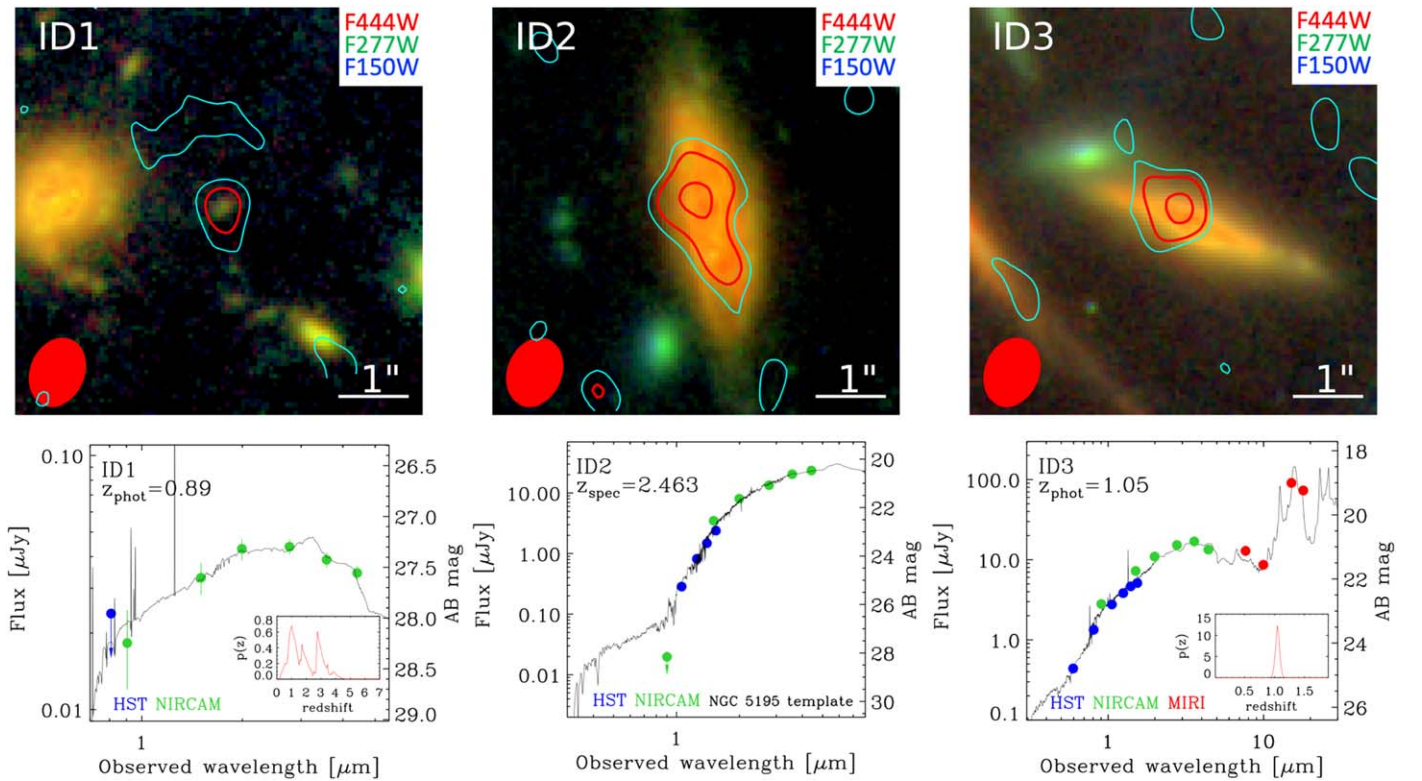


Figure 1. Upper panels: color composite images of the SMGs in this work combining the F150W (blue), F277W (green), and F444W (red) bands. The ALMA continuum is represented by contours in 2σ (cyan) and 3σ , 5σ (red) of the ALMA continuum map noise. The ALMA beams are shown as filled red ellipses of each panel. Bottom panels: best-fit SEDs of our sample. We show the photometry from the Hubble Space Telescope (HST; blue), JWST/NIRCam (green), and JWST/MIRI (red). Since the spec- z of the target ID2 is 2.464, we fit the SED with local galaxy templates (Brown et al. 2014), and find the best-fitted template is the one of NGC 5195. ID1 and ID3 have not been spectroscopically confirmed. Therefore, we estimate the photo- z with EAZY, showing the templates with highest probability, and the $p(z)$ vs. redshift in the subplot panel. The MIRI photometry matches well with the PAHs feature that is predicted by the best-fitted template. ID1 is the faintest target in our sample and the $p(z)$ shows two peaks at $z \sim 0.9$ and 2.9; we further discuss the ID1 photo- z in Section 4.2.

(ALCS, PI: Kotaro Kohno; Kokorev et al. 2022; Sun et al. 2022) in band six (260 GHz, 1.15 mm). Gravitational lensing by the galaxy cluster boosts the background galaxy flux, facilitating the detection of high- z galaxies. Therefore, the combination of the archival data and the MIR data from JWST ERO observations of SMACS 0723 provide us with a very unique chance to study SMGs behind SMACS 0723. We adopt $H_0 = 70 \text{ km s}^{-1} \text{ Mpc}^{-1}$, $\Omega_M = 0.3$, $\Omega_\Lambda = 0.7$, and AB magnitudes (Oke & Gunn 1983) throughout.

2. SMG Sample and Multiwavelength Data Sets

2.1. SMGs from the ALMA Band Six Image

We use archival data for the ALMA band six ALCS observations of SMACS 0723 (Kokorev et al. 2022; Sun et al. 2022). The data were reduced and calibrated using the default SCRIPTFORPLPY script in the Common Astronomy Software Applications (CASA; McMullin et al. 2007). The continuum map is mosaicked by TCLEAN with the parameters GRIDDER = “MOSAIC”, WEIGHTING = “BRIGGS”, ROBUST = 2.0. The final image mosaic reaches an rms of about 0.066 mJy with a beam size of $1''.01 \times 0''.77$, PA = 22° .

To perform the target identification and photometry we used Source Extractor (SExtractor; Bertin & Arnouts 1996) with a detection threshold of 4σ above the background noise on the primary beam uncorrected map, which leads to six targets located within the NIRCam field of view. To validate the target selection, we check the negative image, where one target

is found; this translates into a reliability of $(N_{\text{positive}} - N_{\text{negative}})/N_{\text{positive}} = 83.3\%$. To further validate the results, we use the ALMA coordinates to find NIRCam counterparts within a $0''.5$ search radius. The three objects that have clear NIRCam counterparts are the subject of this paper. We include 10% of the flux as the flux error to account for the calibration uncertainty (Fomalont et al. 2014).

2.2. JWST Data

The JWST ERO contains NIRCam images in F090W, F150W, F200W in the short wavelength channel (SW) and F277W, F356W, and F444W in the long wavelength channel. The public release includes the processed “stage three” images. However, the astrometry with these images is not accurate enough for our study. Therefore, we reprocessed the data based on the “stage two” products. A number of issues with the current JWST data reduction pipeline were fixed, including the pedestal background correction in the SW bands. The final mosaics have the scale of $0''.06 \text{ pix}^{-1}$, and are aligned to the RELICS HST images in pixel coordinates. We also corrected the zero points of NIRCam filters using the STScI calibration CRDS file *jwst_0942.pmap*, which uses the photometric calibration presented in Rigby et al. (2022). The astrometry is tied to Gaia DR2 and is accurate to $\sim 30 \text{ mas}$. We show the NIRCam image cutouts and ALMA contours in Figure 1. This is the first time we resolve the SMG morphology in the rest-frame near-infrared bands; in our sample there are two disk

Table 1
SMG Catalog in SMACS 0723^a

Name	R.A. (J2000)	Decl. (J2000)	Redshift	$S_{260\text{GHz}}$ (mJy)	$\log(M_*)$ (M_\odot)	$\log(\text{SFR})$ ($M_\odot \text{ yr}^{-1}$)	Half-light Radius _{1.1mm} (arcsec)	Half-light Radius _{F444W} (arcsec)	Magnification Factor (μ)
ID1	07:23:15.1	-73:27:46.2	0.89 ^b	0.58 ± 0.06	0.15 ± 0.10	1.36
ID2	07:23:03.9	-73:27:06.1	2.463	1.28 ± 0.13	11.81 ± 0.11	2.10 ± 0.55	0.44 ± 0.25	0.80 ± 0.10	2.08
ID3	07:23:25.1	-73:27:38.9	1.05	0.42 ± 0.04	10.43 ± 0.07	1.37 ± 0.11	0.28 ± 0.22	0.49 ± 0.10	1.69

Notes.

^a The flux, M_* , SFR, and half-light radii values in this table are not corrected by the lensing magnification factor. The typical uncertainty of the magnification factor is 20% (Mahler et al. 2022; Pascale et al. 2022).

^b The photoz and physical parameters for ID1 may not be reliable. This target is more likely to be an SMG at redshift above 4; see Section 4.2.

galaxies (ID2 and ID3) and one faint small galaxy (ID1 with F200W magnitude ~ 27).

SMACS 0723 is also observed by JWST/MIRI in the F770W, F1000W, F1500W, and F1800W bands. Of the three SMGs, only ID3 has a MIRI detection; ID1 is undetected while ID2 is not covered by MIRI. Our new results confirm the photoz measured by Coe et al. (2019) ($z_{\text{phot}} = 0.9820$) and the MIRI observations show good agreement with the presence of polycyclic aromatic hydrocarbons (PAHs) commonly found in dusty star-forming galaxies.

2.3. Lens Model

Recently, Golubchik et al. (2022) published a lens model for SMACS 0723, based on images from the HST and redshifts measured from the Multi Unit Spectroscopic Explorer (Bacon et al. 2010) using the Light-Traces-Mass (LTM) approach (Zitrin et al. 2015). The NIRCcam imaging of SMACS 0723 revealed new multiply imaged galaxies from which updated parametric lensing models were built (Caminha et al. 2022; Mahler et al. 2022; Pascale et al. 2022). In this work, we adopt the average from the LTM model of Golubchik et al. (2022) and the parametric model of Pascale et al. (2022).

3. Properties of the SMGs in This Work

3.1. SMG SED Fitting

We used SExtractor in dual-image mode to measure the photometry for the entire cluster field, using F444W as the detection image.¹⁰ As mentioned in Section 2.2, ID3 is the only target in our sample with both HST and JWST/MIRI detections. Only ID2 has a spectroscopic redshift ($z = 2.463$; Carnall et al. 2022), so we derive the photometric redshifts of ID1 and ID3 using EAZY (Brammer et al. 2008) with the default templates and the local galaxy templates (Brown et al. 2014), which include the PAH features to match the MIRI data of ID3. We include 0.05 mag uncertainty to alleviate potential impact of yet uncertain instrument calibrations.

The EAZY photoz and $p(z)$ curves are shown in Figure 1. For ID2, we fit the SED by the local galaxy templates with spec- z , and find the NGC 5195 template has the minimal χ^2 . NGC 5195 is the dusty minor merger galaxy in the M51 system, implying that ID2's SED is consistent with the dusty emission, though the model predicted F090W is above the observed F090W flux 5σ upper limit.

¹⁰ We did not use the PSF matched photometry because the complex kernel may introduce more noise for the three SMGs. We use the MAG_ISO to ensure a more reliable color measurement for the SED fitting, as well as including most of the flux.

We use the Multi-wavelength Analysis of Galaxy Physical Properties (MAGPHYS) code (da Cunha et al. 2008) to fit the SEDs including the HST, JWST, and ALMA flux simultaneously, and measure the physical properties such as the M_* and SFR (Table 1). The fitting results are shown in Figure A1. The MAGPHYS fit for ID1 shows a level of dust emission higher than the model prediction, suggesting that the EAZY photoz may not be reliable (see Section 4.2), and because of this, we do not list its M_* and SFR in Table 1. In Figure 1 we can see the dust emission contours of ID2 and ID3 are more concentrated toward the galaxy center, while the MAGPHYS dust extinction is assumed as a galaxy-wide average. Given the limited information from the ALMA maps, we adopt the SFR from MAGPHYS. We compare the specific SFR of the main-sequence galaxies ($s\text{SFR}$; M_* , z ; Genzel et al. 2015) and the target ID2 and ID3. The ratio between the $s\text{SFR}$ of our sample and the main-sequence galaxies with their stellar mass and redshift are $s\text{SFR}_{\text{ID2}}/s\text{SFR}_{\text{main sequence}} = 0.23 \pm 0.30$, and $s\text{SFR}_{\text{ID3}}/s\text{SFR}_{\text{main sequence}} = 0.88 \pm 0.29$, implying that ID2 is more likely to be a quiescent galaxy candidate, and ID3 is a main-sequence galaxy at redshift 1.

To characterize the stellar populations, we derive the U , V , J rest-frame magnitudes, and show the $V - J$ versus $U - V$ of ID2 and ID3 in Figure 2. To further reveal the spatial color information resolved by JWST, we measure the photometry inside the central $0''.6$ (~ 5 kpc at redshift 2) to get the central region flux, and estimate the outer disk flux using the measurements beyond $0''.6$. These colors show that the central regions of ID2 and ID3 are dusty. Meanwhile, the disk region of ID3 is more like a star-forming galaxy, while the disk region of ID2 may have been quenched.

3.2. Morphology of This SMG Sample

We also measure the ALMA image sizes of the SMGs using UVMULTIFIT (Martí-Vidal et al. 2014), which fits a Gaussian model in uv space. The deconvolved half-light radius is ~ 2 kpc, which is consistent with the typical SMG dust size, and implies a compact star-forming region at the galaxy center. To compare the stellar mass distribution, we measure the half-light radius of the SMGs from the F444W image, which corresponds to the rest-frame near-infrared band, and is close to the stellar morphology of the SMGs. We correct for the point-spread function (PSF) broadening using $\sigma_{\text{target}}^2 - \sigma_{\text{PSF}}^2$ with the PSF generated by *WebbPSF*.¹¹ Because previous SMG size measurements are mainly based on HST 160W, we compare the HST half-light radius measurements with those of JWST

¹¹ <https://github.com/mperrin/webbpsf>

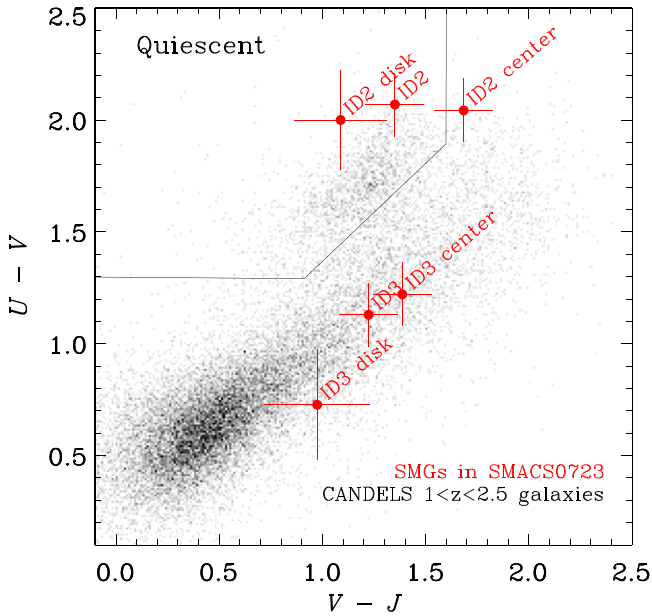


Figure 2. The $V-J$ vs. $U-V$ diagram of our sample. We show the CANDELS (Grogin et al. 2011; Koekemoer et al. 2011) sample at redshifts $1 < z < 2.5$ as a comparison. The solid lines are adopted from Fang et al. (2018) to separate quiescent from star-forming galaxies.

taken in the F150W band. Finally, we correct the galaxy size by dividing the square root of the magnification factor.

The dust size of our sample is shown in Figure 3. Because dust attenuation affects primarily the central parts of galaxies, its presence will bias the half-light radius estimation; the half-light radius increasing as the attenuation in the galaxy center becomes larger. We can see the SMGs in this work also have a concentrated dust distribution, and a larger stellar mass size. Moreover, the F150W half-light radius would be 1.5 times larger than the F444W; thus the stellar distribution size is still large, but may not be as extended as we measured from the HST images.

We also measure the half-light radius of ID3 in the F1500W band, which covers the PAHs feature at redshift 1. Our result shows that the dust size is marginally more extended than the 1.1 mm band size, implying the warm dust from PAHs may be more extended than the cold dust detected by ALMA. Higher resolution ALMA observations are still needed to explore the spatial relation between the PAHs and 1.1 mm emission.

We model the galaxy morphology of ID2 and ID3 in F444W using GALFIT (Peng et al. 2002) and find a Sérsic index ~ 0.9 (Figure A2). The disky structure of ID2 and ID3 indicates that the compact far-IR (FIR emission in the galaxy center cannot be caused by major mergers (Sanders et al. 1988). On the other hand, although both ID2 and ID3 show a disky morphology, the disks themselves display different colors in the UVJ diagram, which may imply different evolutionary paths for high- z disk galaxies.

4. Discussion

4.1. Offset between Submillimeter and NIRCcam

The offset between the ALMA and optical image positions of the SMGs reflects the displacement of the rest-frame UV and FIR, which may be the clumpiness of the star formation region or heavy obscuration by dust (e.g., Cowie et al. 2018). If the dusty starbursts of the SMGs are in the gravitational centers of

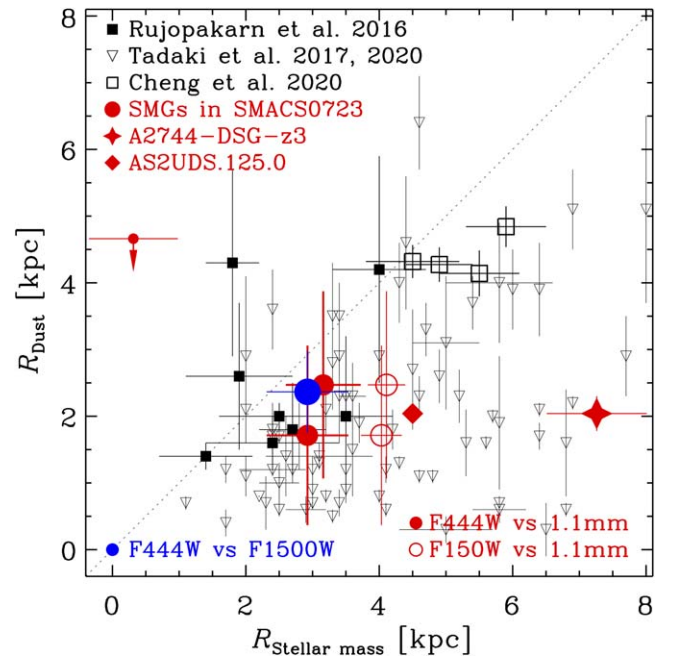


Figure 3. The half-light radius from the NIRCcam F444W image (red points) compared to the dust size from ALMA. We also show the F150W half-light radii (red circles), which are ~ 1.5 times larger than the F444W radii, and the submillimeter galaxy (SMG) size measured from the JWST/NIRCcam images (red diamond and star points; Chen et al. 2022; Wu et al. 2022), or the size measured from HST F140W or F160W images (black points, which is roughly considered as the stellar mass distribution radius; Rujopakarn et al. 2016; Tadaki et al. 2017, 2020; Cheng et al. 2020). The size difference between the F150W and F444W bands may be caused by the dust extinction, and implies that SMGs stellar distribution may be smaller than the size revealed by HST images. The blue circle is the F444W vs. F1500W size for ID3, which measures the extents of regions dominated by the stellar component and the PAH emission at $z \sim 1$.

galaxies, we can expect the stellar mass centers to be better aligned with the dust emission. However, we find that the ID2 and ID3 centers in the F444W image are also offset from ALMA by $\sim 0''.3$ (~ 2.5 kpc at $z = 1.5$). The ALMA pointing accuracy¹² is $P_{\text{acc}} = \text{FWHM}/\text{SNR}/0.9 \approx 0''.1$. If we include the ALMA system offset by $0''.06$ (Ling & Yan 2022) and the NIRCcam World Coordinate Systems (WCS) accuracy $\sim 0''.05$, there is still $\sim 0''.1$ (~ 0.8 kpc at redshift 2) offset between the 1.1 mm and F444W emission (our astrometry is accurate to $\text{rms} = 0''.03$ comparing with Gaia DR2). Minor mergers may explain this offset, as well as the dusty feature in the disky galaxies. Higher resolution ALMA observations are still needed to address the origin of the dusty regions.

4.2. Photoz of ID1: High- z SMGs?

The detection of ID1 by NIRCcam demonstrates the sensitivity of the JWST. The photoz of 0.9 is mainly driven by the peak at F277W and the drop in the F356W and F444W bands, constraining the template peak at rest-frame $1.6 \mu\text{m}$. However, this target is not detected in HST images, and the large error bar of the flux hardly constrains the template fitting. In Figure 4, we show the observed 1.1 mm and the observed Ks band flux ratio versus redshift for the SMGs from the ALMA-GOODS 2.0 survey (Gómez-Guijarro et al. 2022; ALMA-GOODS 2.0) and the templates for SMGs (Arp 220): a star-forming galaxy and a QSO

¹² <https://help.almascience.org/kb/articles/what-is-the-absolute-astrometric-accuracy-of-alm>

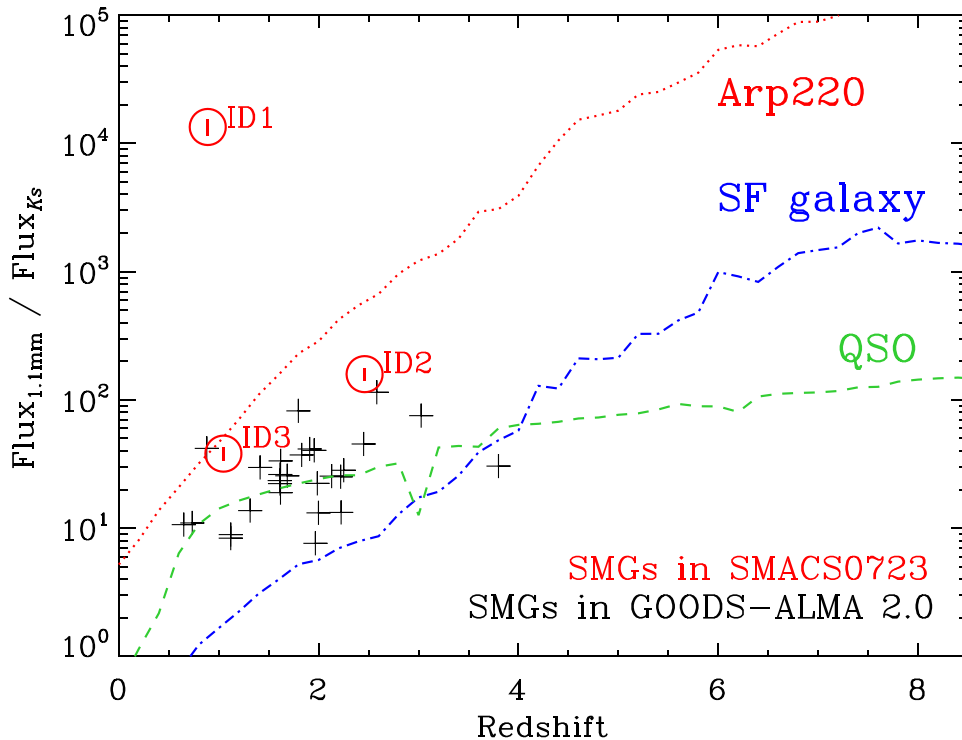


Figure 4. The evolution of the 1.1 mm to Ks observed flux ratio as a function of redshift. We show the submillimeter galaxies (SMGs) from Gómez-Guijarro et al. (2022) (ALMA-GOODS 2.0). The expected trends for a starburst galaxy (Arp 220, dotted red line), a typical star-forming galaxy (dotted-dashed blue line), and a QSO (dashed green line). Both ID2 and ID3 follow the trend of Arp 220 well, but ID1 shows a flux ratio that is too high, suggesting a high- z nature of this target.

template from Polletta et al. (2007). This figure directly shows the possible redshift range based on the observed flux ratio. We can see the 1.1 mm Ks^{-1} 1.1 mm and Ks flux ratio of ID1 is too high at redshift 0.9, and should be at $z > 4$, which is also consistent with the red color at F090W–F200. On the other hand, visual examination of JWST images has revealed that ID1 is located along the direction of a bright star spike. This in return might contaminate the photometry, and result in erroneous interpretation of the redshift and physical parameters.

5. Summary

We present the first study of ALMA detected SMG hosts based on the rest-frame near-infrared (NIR) data from JWST. While our limited sample contains only three objects, we have obtained some “first look” results of the SMGs. We find one object previously undetected by HST, and there is a hint from its millimeter-to-NIR flux ratio that it could be at $z \gtrsim 4$. The other two objects are disk galaxies, one of which seems to have spiral arms. This suggests that their star formation activity is taking place in the secular mode instead of being triggered by major mergers. This conclusion is corroborated by the SED analysis, which shows these galaxies as being on or below the star formation main sequence. The high resolution NIRCcam images also show that their dust emission regions are concentrated to the central regions of the hosts. Consequently, their rest-frame NIR images are more compact than in the rest-frame optical, as NIR light suffers less dust extinction. This reveals a potential bias in the optical-based studies of the stellar mass distribution within galaxies. Lastly, we show that these two galaxies are dramatically different beyond the dust emission regions and that one has a star-forming disk while the other has a quiescent disk. However, further studies of the NIR properties of SMG hosts in statistically significant samples are still necessary to reveal the nature of these objects.

We thank the referee for the kind and constructive comments that helped us to improve the manuscript. C.C. thanks Fengwu Sun, Lixin Yu, Lei Zhu for helpful discussions. We are grateful to the JWST ERO teams for doing the observations and for the prompt data release. This work is supported by the National Natural Science Foundation of China, Nos. 11803044, 11933003, 12173045. This work is sponsored (in part) by the Chinese Academy of Sciences (CAS), through a grant to the CAS South America Center for Astronomy (CASSACA). We acknowledge the science research grants from the China Manned Space Project with No. CMS-CSST-2021-A05. C.N.A.W. acknowledges support from the NIRCcam Development Contract NAS5-02105 from NASA Goddard Space Flight Center to the University of Arizona.

Some/all of the data presented in this paper were obtained from the Mikulski Archive for Space Telescopes (MAST) at the Space Telescope Science Institute. The specific observations analyzed can be accessed via doi: [10.17909/4wr8-hh69](https://doi.org/10.17909/4wr8-hh69). STScI is operated by the Association of Universities for Research in Astronomy, Inc., under NASA contract NAS526555. Support to MAST for these data is provided by the NASA Office of Space Science via grant NAG57584 and by other grants and contracts.

This paper makes use of the following ALMA data: ADS/JAO.ALMA#2018.1.00035.L. ALMA is a partnership of ESO (representing its member states), NSF (USA) and NINS (Japan), together with NRC (Canada), MOST and ASIAA (Taiwan), and KASI (Republic of Korea), in cooperation with the Republic of Chile. The Joint ALMA Observatory is operated by ESO, AUI/NRAO, and NAOJ. The National Radio Astronomy Observatory is a facility of the National Science Foundation operated under cooperative agreement by Associated Universities, Inc. The ALMA data reduction and other data services of this work are fully or partially supported by China-Chile Astronomical Data

Center (CCADC), which is affiliated to Chinese Academy of Sciences South America Center for Astronomy (CASSACA).

Facilities: HST (ACS, WFC3-IR), JWST (NIRCAM, MIRI), ALMA (band6).

Software: astropy (Astropy Collaboration et al. 2013, 2018), Source Extractor (Bertin & Arnouts 1996), GALFIT (Peng et al. 2002), EAZY (Brammer et al. 2008), CASA (McMullin et al.

2007), MAGPHYS (da Cunha et al. 2008), uvmultifit (Martí-Vidal et al. 2014).

Appendix

We show the MAGPHYS SED fitting results in Figure A1 and the GALFIT fitting results in Figure A2.

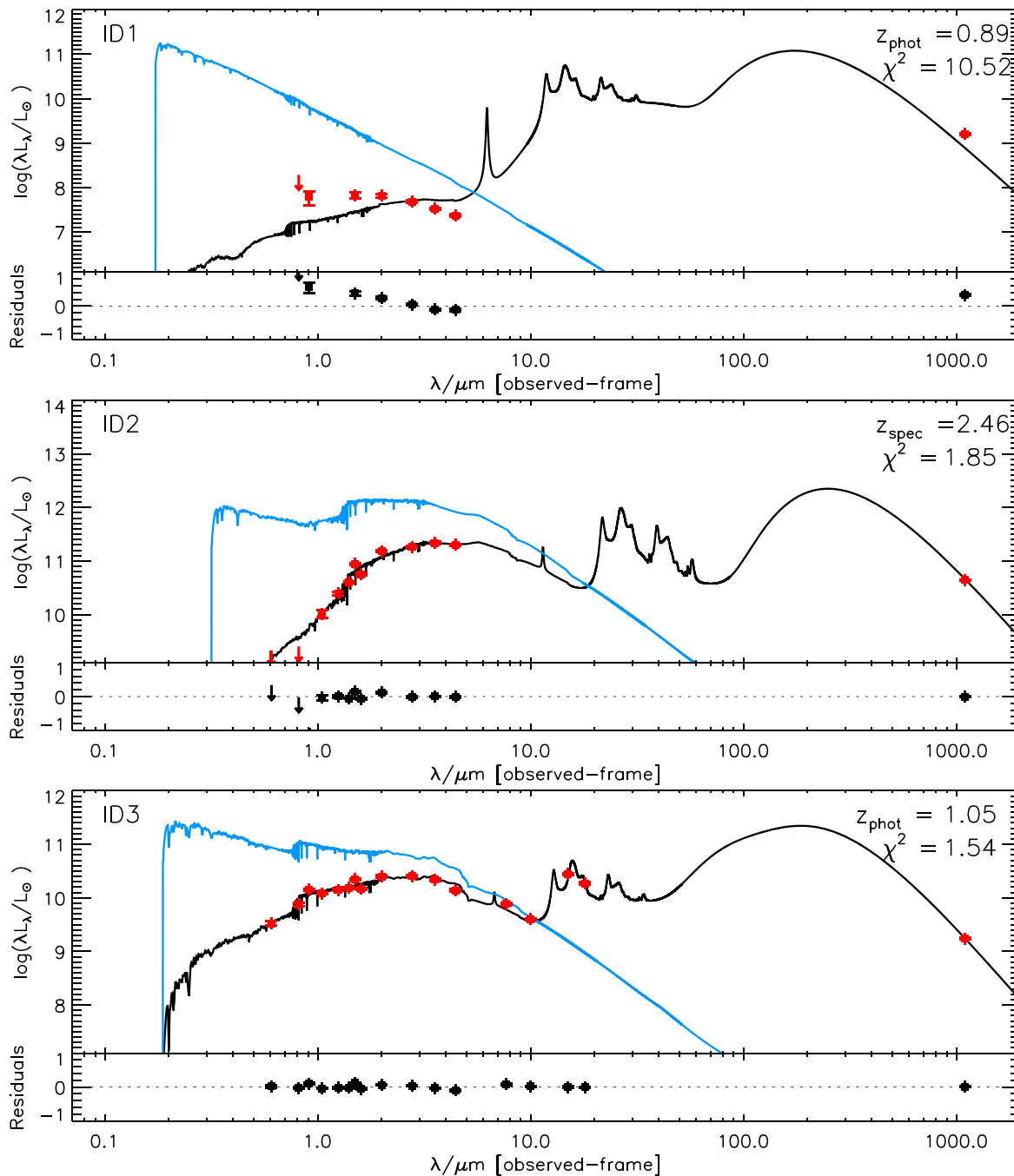


Figure A1. SED fitting results given by MAGPHYS with the observed data (red), best-fitted model (black), and the stellar model (blue) before dust extinction, and the residual in each bottom panel.

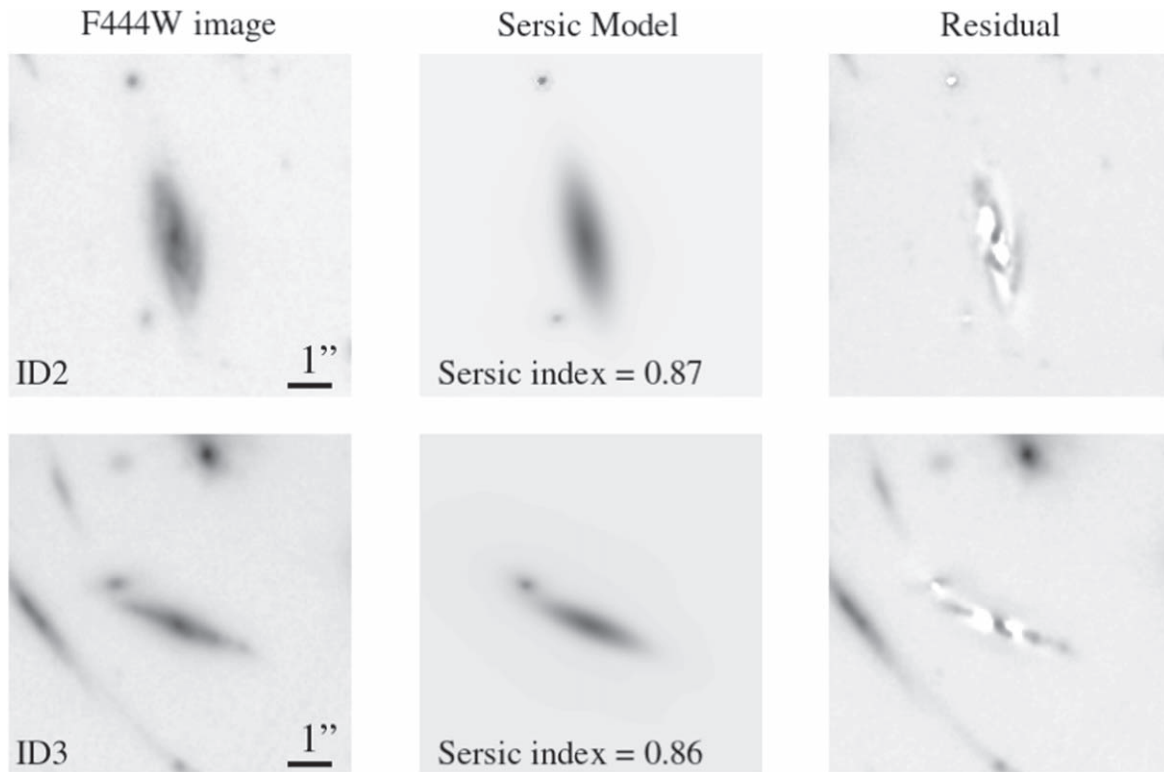


Figure A2. The NIRCcam F444W image (left panel), best fitted by a Sérsic model (central panel) and the fit residual (right panel) of ID2 and ID3.

ORCID iDs

Cheng Cheng <https://orcid.org/0000-0003-0202-0534>
 Haojing Yan <https://orcid.org/0000-0001-7592-7714>
 Jia-Sheng Huang <https://orcid.org/0000-0001-6511-8745>
 Christopher N. A. Willmer <https://orcid.org/0000-0001-9262-9997>
 Zhiyuan Ma <https://orcid.org/0000-0003-3270-6844>
 Gustavo Orellana-González <https://orcid.org/0000-0002-6642-7483>

References

- Astropy Collaboration, Price-Whelan, A. M., Sipőcz, B. M., et al. 2018, *AJ*, **156**, 123
- Astropy Collaboration, Robitaille, T. P., Tollerud, E. J., et al. 2013, *A&A*, **558**, A33
- Bacon, R., Accardo, M., Adjali, L., et al. 2010, *Proc. SPIE*, **7735**, 773508
- Barger, A. J., Cowie, L. L., Chen, C. C., et al. 2014, *ApJ*, **784**, 9
- Bertin, E., & Arnouts, S. 1996, *A&AS*, **117**, 393
- Blain, A. W., Smail, I., Ivison, R. J., Kneib, J. P., & Frayer, D. T. 2002, *PhR*, **369**, 111
- Brammer, G. B., van Dokkum, P. G., & Coppi, P. 2008, *ApJ*, **686**, 1503
- Brown, M. J. I., Moustakas, J., Smith, J. D. T., et al. 2014, *ApJS*, **212**, 18
- Caminha, G. B., Suyu, S. H., Mercurio, A., et al. 2022, arXiv:2207.07567
- Carnall, A. C., Begley, R., McLeod, D. J., et al. 2022, arXiv:2207.08778
- Casey, C. M., Narayanan, D., & Cooray, A. 2014, *PhR*, **541**, 45
- Chen, C.-C., Gao, Z.-K., Hsu, Q.-N., et al. 2022, arXiv:2208.05296
- Cheng, C., Ibar, E., Smail, I., et al. 2020, *MNRAS*, **499**, 5241
- Coe, D., Salmon, B., Bradač, M., et al. 2019, *ApJ*, **884**, 85
- Cowie, L. L., González-López, J., Barger, A. J., et al. 2018, *ApJ*, **865**, 106
- da Cunha, E., Charlot, S., & Elbaz, D. 2008, *MNRAS*, **388**, 1595
- Dudzevičiūtė, U., Smail, I., Swinbank, A. M., et al. 2020, *MNRAS*, **494**, 3828
- Fang, J. J., Faber, S. M., Koo, D. C., et al. 2018, *ApJ*, **858**, 100
- Fomalont, E., van Kempen, T., Kneissl, R., et al. 2014, *Msngr*, **155**, 19
- Fujimoto, S., Ouchi, M., Shibuya, T., & Nagai, H. 2017, *ApJ*, **850**, 83
- Genzel, R., Tacconi, L. J., Lutz, D., et al. 2015, *ApJ*, **800**, 20
- Golubchik, M., Furtak, L. J., Meena, A. K., & Zitrin, A. 2022, arXiv:2207.05007
- Gómez-Guijarro, C., Elbaz, D., Xiao, M., et al. 2022, *A&A*, **658**, A43
- Grogin, N. A., Kocevski, D. D., Faber, S. M., et al. 2011, *ApJS*, **197**, 35
- Gullberg, B., Smail, I., Swinbank, A. M., et al. 2019, *MNRAS*, **490**, 4956
- Koekemoer, A. M., Faber, S. M., Ferguson, H. C., et al. 2011, *ApJS*, **197**, 36
- Kokorev, V., Brammer, G., Fujimoto, S., et al. 2022, arXiv:2207.07125
- Ling, C., & Yan, H. 2022, *ApJ*, **929**, 40
- Mahler, G., Jauzac, M., Richard, J., et al. 2022, arXiv:2207.07101
- Martí-Vidal, I., Vlemmings, W. H. T., Müller, S., & Casey, S. 2014, *A&A*, **563**, A136
- McMullin, J. P., Waters, B., Schiebel, D., Young, W., & Golap, K. 2007, in *ASP Conf. Ser. 376, Astronomical Data Analysis Software and Systems XVI*, ed. R. A. Shaw, F. Hill, & D. J. Bell (San Francisco, CA: ASP), **127**
- Oke, J. B., & Gunn, J. E. 1983, *ApJ*, **266**, 713
- Pascale, M., Frye, B., Diego, J., et al. 2022, arXiv:2207.07102
- Peng, C. Y., Ho, L. C., Impey, C. D., & Rix, H.-W. 2002, *AJ*, **124**, 266
- Polletta, M., Täger, M., Maraschi, L., et al. 2007, *ApJ*, **663**, 81
- Pontoppidan, K., Blome, C., Braun, H., et al. 2022, arXiv:2207.13067
- Riechers, D. A., Capak, P. L., Carilli, C. L., et al. 2010, *ApJL*, **720**, L131
- Rigby, J., Perrin, M., McElwain, M., et al. 2022, arXiv:2207.05632
- Rujopakarn, W., Dunlop, J. S., Rieke, G. H., et al. 2016, *ApJ*, **833**, 12
- Sanders, D. B., Soifer, B. T., Elias, J. H., et al. 1988, *ApJ*, **325**, 74
- Shanks, T., Ansarnejad, B., Bielby, R. M., et al. 2021, *MNRAS*, **505**, 1509
- Smail, I., Ivison, R. J., Blain, A. W., & Kneib, J. P. 1998, *ApJL*, **507**, L21
- Sun, F., Egami, E., Fujimoto, S., et al. 2022, *ApJ*, **932**, 77
- Tacconi, L. J., Neri, R., Chapman, S. C., et al. 2006, *ApJ*, **640**, 228
- Tadaki, K.-i., Belli, S., Burkert, A., et al. 2020, *ApJ*, **901**, 74
- Tadaki, K.-i., Genzel, R., Kodama, T., et al. 2017, *ApJ*, **834**, 135
- Toft, S., Smolčić, V., Magnelli, B., et al. 2014, *ApJ*, **782**, 68
- Ueda, Y., Hatsukade, B., Kohno, K., et al. 2018, *ApJ*, **853**, 24
- Wu, Y., Cai, Z., Sun, F., et al. 2022, arXiv:2208.08473
- Zitrin, A., Fabris, A., Merten, J., et al. 2015, *ApJ*, **801**, 44